

GAS SLOSHING AND BUBBLES IN THE GALAXY GROUP NGC 5098

S. W. RANDALL¹, C. JONES¹, M. MARKEVITCH¹, E. L. BLANTON², P. E. J. NULSEN¹, W. R. FORMAN¹

Astrophysical Journal, accepted

ABSTRACT

We present results from *Chandra* observations of the galaxy pair and associated galaxy group NGC 5098, and find evidence for both gas sloshing and AGN heating. The X-ray brightness images show diffuse emission with a spiral structure, centered on NGC 5098a, and a sharp edge in the diffuse emission surrounding much of the galaxy at about 30 kpc. The spiral structure in the X-ray surface brightness and temperature maps, the offset between the peak of the cool gas and the central AGN, and the structure of the cold front edges all suggest gas sloshing in the core. The most likely perturber is the nearby galaxy NGC 5098b, which has been stripped of its gaseous atmosphere. Detailed images of the core reveal several X-ray cavities, two of which, just north and southeast of the central AGN, correlate with radio emission and have bright X-ray rims, similar to buoyant bubbles seen in the ICM of other systems. We estimate the pressures in the bubbles and rims and show that they are roughly equal, consistent with these being young features, as suggested by their close proximity to the central AGN. We assume that the other X-ray cavities in the core, which show no correlation with existing radio observations, are ghost cavities from previous AGN outbursts. An estimate of the mechanical energy required to inflate the cavities indicates that it is sufficient to offset radiative cooling of the gas for 15 Myr. Therefore, for a typical cycle time of 10^7 yrs, the central AGN energy output is enough to balance cooling over long timescales.

Subject headings: galaxies: clusters: general — galaxies: clusters: individual (RGH80, NSCS J132014+330824) — X-rays: galaxies — galaxies: individual (NGC5098)

1. INTRODUCTION

A major surprise from early *Chandra* and *XMM-Newton* observations was that gas in cool core clusters does not reach the low central temperatures predicted by radiative cooling models, in disagreement with the previously accepted cooling flow model (Peterson & Fabian 2006). The implication is that the central gas must experience some kind of heating. The source of this heating, and understanding when and how it takes place, has recently been a major topic of study in extragalactic astrophysics. A promising candidate is feedback from energy injection by the central AGN of the cD galaxy (McNamara & Nulsen 2007). However, the details of this interaction, and how the energy is transferred from the jets to the ambient ICM, are poorly understood. Galaxy groups provide an excellent opportunity to study heating and other non-gravitational processes in the ICM. Although not as X-ray luminous as clusters, the effects of heating are more readily seen in groups, due to their lower mass and central density. For example, the gas fraction in groups shows a relatively large scatter (~ 2 at any fixed temperature) within r_{2500} , with the scatter being tightly correlated with the central entropy (Gastaldello et al. 2007; Sun et al. 2009), reflecting the greater role of non-gravitational processes in the centers of groups as compared to clusters.

Another discovery from *Chandra* was the existence of contact discontinuities, or cold fronts, where a cool, dense

subclump of gas exhibits a temperature and density jump at the interface with warmer gas, such that the pressure profile across the interface is continuous (Markevitch & Vikhlinin 2007). More recently, it has been shown that such cold fronts can be generated not only from subgroup cores in a merger, but also by gas sloshing around a potential minimum, caused by an off-axis interaction with a perturber (Ascasibar & Markevitch 2006). Cold fronts are found in clusters and groups with relatively high frequency, and sloshing cold fronts have been identified in a handful of systems (e.g., Mazzotta et al. 2001; Dupke et al. 2007; Gastaldello et al. 2009). Understanding cold fronts and sloshing is of interest as they can have a significant impact on cluster cores through gas heating, ICM mixing and enrichment, turbulence, constraints on conduction and magnetic fields, etc.

In this paper we report on *Chandra* observations of the NGC 5098 galaxy group (RGH 80), originally identified by Ramella et al. (1989), which shows evidence for both AGN heating and gas sloshing. Studies of *ROSAT* and *ASCA* observations found average temperatures and metallicities for this system of ~ 1 keV and $\sim 30\%$ solar (Davis et al. 1999; Hwang et al. 1999; Buote 2000; Mahdavi et al. 2000). More recently, *XMM-Newton* observations were used to derive radial profiles for various properties of the X-ray gas, including temperature, pressure, entropy, total mass, gas mass, and cooling time (Xue et al. 2004; Mahdavi et al. 2005). A joint analysis of the *XMM-Newton* and *Chandra* data we consider here was performed by Gastaldello et al. (2007) as part of a sample of relaxed galaxy groups. The *Chandra* data were used to study the global properties of the gas in this system as part of the group sample studied by Sun et al. (2009). X-ray observations imply a total group mass of

¹ Harvard-Smithsonian Center for Astrophysics, 60 Garden St., Cambridge, MA 02138, USA; srandall@cfa.harvard.edu, cjf@cfa.harvard.edu, mmarkevitch@cfa.harvard.edu, wrf@cfa.harvard.edu

² Institute for Astrophysical Research, Boston University, 725 Commonwealth Ave., Boston, MA 02215, USA; eblanton@bu.edu

$4 - 6 \times 10^{13} M_{\odot}$, and optical studies find a group line-of-sight velocity dispersion of $\sigma_{\text{los}} = 602 \text{ km s}^{-1}$ (Xue et al. 2004; Mahdavi et al. 2005).

The NGC 5098 galaxy group is dominated by the central galaxy pair NGC 5098a and NGC 5098b (first identified by Ramella et al. 1995, their “group 80”). NGC 5098a is the brighter (and presumably larger) of the two, with absolute optical magnitudes of $M_B = -21.131$ and $M_V = -22.097$, as compared to $M_B = -20.845$ and $M_V = -21.770$ for NGC 5098b. Absolute magnitudes were calculated from magnitudes given in the Sloan Digital Sky Survey (SDSS; Adelman-McCarthy et al. 2008) catalog and transformed to the Johnson filter system using the relations provided by Smith et al. (2002). The relative line-of-sight velocity of the pair is 360 km s^{-1} , slightly less than the group velocity dispersion. The western galaxy, NGC 5098a, hosts the extended radio source B2 1317+33, which has been detected at several frequencies (Colla et al. 1970; Parma et al. 1986; Morganti et al. 1997; Condon et al. 1998).

We report here on *Chandra* observations of NGC 5098. As the global structure of the gas has already been studied using *XMM-Newton* (Xue et al. 2004) and *Chandra* (Sun et al. 2009), we focus on detailed structure in the central regions, a task for which *Chandra* is well-suited. The observations and data reduction techniques are described in § 2. The X-ray image is presented in § 3, and results on temperature and abundance structure from spectral analysis are given in § 4. In § 5, we argue that the central gas is currently sloshing due to a recent interaction with a nearby galaxy, most likely with NGC 5098b. We also report on the detection of several X-ray cavities in the central region and use these to show that the energy output by the central AGN is sufficient to balance radiative cooling of the gas. Our results are summarized in § 6.

We assume an angular diameter distance to NGC 5098 of 153.1 Mpc, which gives a scale of $0.74 \text{ kpc}''$ for $\Omega_0 = 0.3$, $\Omega_{\Lambda} = 0.7$, and $H_0 = 70 \text{ km s}^{-1} \text{ Mpc}^{-1}$. All error ranges are 68% confidence intervals (i.e., $1-\sigma$), unless otherwise stated.

2. OBSERVATIONS AND DATA REDUCTION

NGC 5098 was originally observed with *Chandra* on August 4, 2001, for 11 ksec with the *Chandra* CCD Imaging Spectrometer (ACIS) in Very Faint mode, pointed such that the galaxy was visible on the front-side illuminated ACIS-I CCD array. It was again observed on November 5, 2005, for 39 ksec with ACIS in Very Faint mode, pointed such that the galaxy was visible on the back-side illuminated ACIS-S3 CCD. Due to the longer exposure time and better sensitivity at soft energies, we considered only data from the more recent ACIS-S3 observation. These data were reduced using the method described in Randall et al. (2008). All data were reprocessed from the level 1 event files using the latest calibration files (as of CIAO4.0). CTI and time-dependent gain corrections were applied where applicable. LC_CLEAN was used to remove background flares³. The mean event rate was calculated using time bins within 3σ of the overall mean, and bins outside a factor of 1.2 of this mean

were discarded. The resulting cleaned exposure time was 38.4 ksec.

The emission from NGC5098 and the surrounding group fills the ACIS-S3 image field of view. We therefore used the standard CALDB⁴ blank sky background files appropriate for each observation, normalized to our observations from the ACIS-S1 chip in the 10-12 keV energy band. To generate exposure maps, we assumed a MEKAL model with $kT = 1 \text{ keV}$, Galactic absorption, and abundance of 30% solar at a redshift $z = 0.0379$, which is consistent with typical results from detailed spectral fits (see § 4).

3. THE X-RAY IMAGE

The exposure corrected, background subtracted, smoothed image is shown in Figure 1 (the optical *DSS* image of the same field is shown for comparison). The image shows several interesting features associated with NGC 5098a:

- A bright point source, coincident with the central AGN, near the center of the diffuse emission.
- A plume of emission extending to the northeast (the “tail” noted previously by Gastaldello et al. 2007). The plume exhibits a spiral arm morphology, originating east of NGC 5098a and wrapping around to the north. The presence of this feature indicates that the system is not dynamically relaxed. NGC 5098a is most likely currently interacting with NGC 5098b.
- A sharp surface brightness edge to the west, southwest, and south, roughly $30''$ (28 kpc) from the central AGN. The edge appears to continue to the east and define the outer boundary of the arm, adding to the overall impression of a spiral pattern in the diffuse emission. The edges are similar to features seen from cold fronts generated by gas sloshing in observations (Dupke et al. 2007; Gastaldello et al. 2009) and simulations (Ascasibar & Markevitch 2006) of galaxy clusters and groups.
- An asymmetry in the brightest (central) diffuse emission, which extends farther west of the AGN than to the east, also suggesting that this system is disturbed.
- Two small cavities, surrounded by bright rims of emission, roughly $4''$ (3 kpc) to the north and southwest of the AGN. They are morphologically similar to “bubbles” seen in X-ray observations of other galaxies and clusters, some of which are associated with radio emission (e.g., Abell 2052, Blanton et al. 2003; Perseus cluster, Fabian et al. 2006; NGC 4552, Machacek et al. 2006; MS0735.6+7421, McNamara et al. 2007; M84, Finoguenov et al. 2008; NGC 5044, Gastaldello et al. 2009), though they are relatively small in size. The proximity of the bubbles to the AGN suggests that they are young features, possibly currently being inflated by jets from the AGN.

³ <http://asc.harvard.edu/contrib/maxim/acisbg/>

⁴ <http://cxc.harvard.edu/caldb/>

Also of note is the complete lack of X-ray emission associated with NGC 5098b. Although the galaxy is well within the northeastern arm of NGC 5098a, there is no indication of enhanced surface brightness centered on the galaxy. This suggests that NGC 5098b may have been stripped of its gas during an interaction with NGC 5098a or the ambient group ICM.

In order to examine the faint, diffuse, group emission at larger radii, we made a more heavily smoothed image, shown in Figure 2. Point sources have been removed by filling in source regions using a Poisson distribution whose mean was equal to that of a local annular background region. Diffuse emission is seen beyond the core and the edges noted in Figure 1, in all directions. The extended halo also shows hints of a spiral structure, continuing from the inner arm noted in Figure 1 and wrapping around from the north out to a radius of $\sim 120''$ (89 kpc), through the west, and back to the south out to $\sim 132''$ (98 kpc), though the reality of this structure is unclear, and may just be an artifact of the brighter, inner arm reaching into the extended emission in the north. There appears to be a sharp, linear edge in the extended emission to the south. The orientation of the edge is such that it cannot be due to a chip node boundary. We searched the NASA/IPAC Extragalactic Database for a foreground absorber that could be responsible for this feature, but found none. To the southwest, there is an extended source associated with the galaxy triplet NGC 5096, which has been included as a member of the NGC 5098 group (Ramella et al. 1995). Using optical and *XMM-Newton* X-ray observations, Mahdavi et al. (2005) identify this source as an independent subgroup that has not yet interacted with, nor is bound to, the main group.

3.1. Unsharp-Masked Image

To better visualize faint surface brightness fluctuations, particularly near the core, we made a (0.3–5.0 keV) unsharp-masked image. It was created by dividing the image smoothed with a $0.98''$ radius Gaussian by one smoothed with a $9.8''$ Gaussian. The resulting image is shown in Figure 3. Two bubbles are clearly seen to the north and southeast of the central AGN, which are also detected in the radio (see Figure 4). The surface brightness profiles in four sectors, two of which contain the bubbles, are compared to the average profile in Figure 5. This figure shows that the northern and southern bubbles correspond to $\sim 60\%$ and $\sim 40\%$ deficits respectively, as compared to both the average profile and the peaks at larger radii which correspond to the bright X-ray rims. In the radio, 6 cm observations clearly show a central core with two radio lobes corresponding to the bubbles seen in the *Chandra* images, with comparable radio flux from each lobe and the core (see B2 1317+33 in Morganti et al. 1997). In Figure 4 we overlay radio contours from VLA L-band 1.45 GHz data taken from the VLA image archive over a close-up of the core in Figure 3. Radio emission fills the X-ray bubbles.

The unsharp-masked image also reveals complex structure in the diffuse emission, most notably southwest of the AGN, with several surface brightness depressions similar to those seen in the bubbles (but without the surrounding bright rims), all within the outer edge noted in Figure 1. There is no obvious correlation between the ra-

dio observations and these other X-ray cavities. A comparison of the net counts in these depressions to those from adjacent regions shows that most are statistically significant at the $2\text{--}3\sigma$ level. In the bubbles, the count rates in the rims are higher than those in the central depressions by 4.6σ and 2.3σ , for the northern and southern bubbles respectively. For one of the more significant cavities to the southwest, the deficit is significant at 3.8σ . Therefore, the statistical significance of the cavities is on the order of that for the bubbles, which are seen in the radio and clearly real features. The large, dark region to the east, just outside the bubbles, is an artifact of the relatively sharp drop-off in surface brightness in this region, possibly indicating an edge in the central bright diffuse emission (although the bright rims of the bubbles also contribute to this deficit).

4. SPECTRAL ANALYSIS

The X-ray image (Figure 1) shows diffuse emission associated with NGC 5098a, as well as fainter group emission filling the field of view. We generated a temperature map as a guide for detailed spectral fitting to disentangle the various components and study the structure seen in the ICM. We assume a galactic absorption of $N_H = 1.31 \times 10^{20} \text{ cm}^{-2}$ throughout.

4.1. Temperature Map

The temperature map was derived using the same method as developed in Randall et al. (2008; 2009). For each temperature map pixel, we extracted a spectrum from a circular region containing 1000 net counts (after subtracting the blank sky background). The resulting spectrum was fit in the 0.6 – 5.0 keV range with an absorbed APEC model using XSPEC, with the abundance allowed to vary. The resulting temperature map, with X-ray surface brightness contours overlaid, is shown in Figure 6. Unfortunately, due to the small number of net counts, the extraction regions for the temperature map pixels were relatively large. Faint regions had extraction radii on the order of $1.6'$ (71 kpc), while the brightest regions, near the core of NGC 5098a, had radii of $7.9''$ (5.8 kpc). As a result, each pixel in the temperature map is highly correlated with nearby pixels, and the temperature map is effectively smoothed on large scales, particularly in regions far from the core.

Nevertheless, there are several interesting features in the temperature map. There is an elliptical clump of cool gas west of the AGN, which appears to be doubly peaked to the north and south. The cool gas wraps around the AGN, but does not overlap it. The outer edge of this cool region roughly corresponds to the surface brightness edge noted in Figure 1, suggesting that this feature is a cold front. A long arm of cool gas extends east of the AGN and wraps around to the north, with the outer edge connecting to the edge of the cool elliptical region in the south. The orientation and morphology of the cool arm is very similar to the arm seen in the surface brightness map (Figure 1), though it extends well beyond the apparent outer boundary of the surface brightness arm. We investigate this feature further in § 4.2. As in the surface brightness map, there is no structure correlated with NGC 5098b. As a test of the robustness of the temperature measurements in faint regions, we re-fit the spectra for a few temperature map pixels near the tip of the cool

arm in the temperature map and varied the background normalization by $\pm 10\%$. We found no significant effect on the resulting temperature. The average radial temperature structure is consistent with that found previously from analyses of *Chandra* and *XMM-Newton* data (Xue et al. 2004; Gastaldello et al. 2007), with $kT \approx 0.8$ keV near the core of NGC 5098a, rising to ~ 1.3 keV at 1.5–2' (67–89 kpc), and dropping off at larger radii.

To search for correlation with the detailed structure shown in Figure 3, we made a higher-resolution temperature map of the central region of NGC 5098a, shown in Figure 7, with the same X-ray surface brightness contours as in Figure 6. The smoothing scales are too large to show any structure at the level of the X-ray cavities shown in Figure 3, although the double-peaked nature of the elliptical region, and its anti-correlation with the AGN, can be seen more clearly. It is also clear that the temperature in the inter-arm region, between the arm's inner edge and the cooler central gas, is consistent with the ambient temperature of ~ 1.2 keV. This is also consistent with what we find from detailed spectral fits (see § 4.2).

The structure of the temperature map, in particular the cool spiral arm morphology and the offset of the cool gas from the central AGN, supports our conclusion from § 3 that this is a disturbed system, possibly due to an interaction with the nearby galaxy NGC 5098b. In particular, these features are very similar to those seen from sloshing of the central gas about the potential minimum (see Figure 7 in Ascasibar & Markevitch 2006, especially at 1.7 - 1.9 Gyr). We discuss this possibility further in § 5.

4.2. Detailed Spectra

4.2.1. Diffuse Emission

Based on the derived temperature map and the X-ray image, we defined 7 regions for detailed spectral analysis. A summary of the spectral model for each region is given in Table 1. R1 is centered on the AGN and covers the central projected $26''$ (19.2 kpc) of NGC 5098a. R2 and R3 correspond to the southern and northern cool spots in the larger elliptical region of cool gas seen in the temperature map, respectively. R4 covers the inner part of the cool arm seen in the temperature map, while the adjacent region R5 is the hotter area just outside of the temperature map arm (though R5 overlaps with the arm seen in the surface brightness map). The regions are shown overlaid on the X-ray image and temperature map in Figure 8, where in the left panel point sources have been removed as in Figure 2.

A single-temperature thermal model was an adequate fit to each region considered in Table 1. The best-fitting temperature for the “inter-arm” region seen in the temperature map (R5) was greater than that in the adjacent region R4, with a significance of 3.7σ . The best-fitting abundance was also higher in R5, by more than a factor of two. As a test, we re-fit the spectrum from R5 with the abundance fixed to the best-fitting value from region R4 (row 6 in Table 1). The chi-squared per degree-of-freedom was significantly worsened by fixing the abundance, and the best-fitting temperature was still found to be higher, with a significance of 2.3σ . This suggests that the arm structure seen in the temperature map in

the vicinity of R4 and R5 is real, and not an artifact of smoothing.

As noted in § 4.1, the cool arm seen in the temperature map extends beyond the outer edge of the arm in the surface brightness map. R6 and R7 were defined to evaluate the significance of the temperature difference in these regions. Table 1 shows that the best-fitting temperature in R7 is higher than that in R6 with high significance (greater than 6σ). This confirms that the emission near the edge of the FOV is hotter northwest of the AGN as compared to the northeast, as suggested by the arm feature in the temperature map, independent of smoothing effects.

4.2.2. The Surface Brightness Edges

The surface brightness edges indicated in Figure 1 are similar to features arising from contact discontinuities, or “cold fronts”, seen in simulations and observations of galaxy clusters and groups (e.g., Ascasibar & Markevitch 2006; Dupke et al. 2007; Gastaldello et al. 2009). We therefore extracted spectra across these edges to search for temperature jumps, which are characteristic of cold fronts. Spectra were extracted from the same semi-annular regions shown in Figure 10, but with fewer (larger) radial bins, such that each bin contained ~ 500 net counts. The resulting spectra were fit with a single temperature APEC model, with the abundance allowed to vary. The resulting temperature profiles are shown in Figure 9. Each profile shows a clear jump at the location of the apparent surface brightness edge, identifying these features as cold fronts. These features are discussed in more detail in § 5.1. We note that, for the northeastern profile, the elevated temperature of the innermost bin (which overlaps with region R5 in Figure 8) and the lower temperatures at large radii (as compared to the southwestern profile) are consistent with what is shown the temperature map (Figure 6).

4.2.3. The Central Source

We extracted a spectrum for the central source in NGC 5098a using an aperture with a radius of $1.8''$. The background was determined locally from an annulus centered on the source with inner and outer radii of $1.8''$ and $4.0''$, respectively. This gave 264 net counts in the 0.6 – 7.0 keV band. The spectrum was fit with an absorbed power-law, giving a best-fitting photon index of 1.93 ± 0.16 , which is typical for a radio galaxy (e.g., Sambruna et al. 1999). The source has an unabsorbed flux of 4.2×10^{-14} ergs cm^{-2} s^{-1} and X-ray luminosity of 1.4×10^{41} ergs s^{-1} in the 0.6 – 7.0 keV energy band. We also fit the spectrum with the XSPEC intrinsic absorption model ZWABS and find that the spectrum is consistent with no internal absorption.

5. DISCUSSION

5.1. Structure of the Cold Fronts

The *Chandra* image (Figure 1) shows a brightness edge almost completely encircling NGC 5098a. It is sharpest and closest in the west/southwest, continues on to the south, and spirals out to form the outer boundary of the surface brightness arm in the northeast. Spectral analysis revealed temperature jumps across each edge, indicating that these edges are cold fronts (§ 4.2.2). As such, we

expect there to be a density discontinuity located at each edge. To measure the amplitude of these density jumps, we extracted the *Chandra* 0.6–5.0 keV surface brightness profile in two sectors, one to the southwest and another to the northeast. The regions were defined such that the radii of curvature matched those of the edges. In each case, the center of curvature was reasonably close to the peak of the diffuse X-ray emission, near the central AGN. The extraction regions are shown in Figure 10.

The resulting emission measure profiles are shown in Figure 11 (distance is measured from the center of curvature of the apparent edge). These profiles were fit with a spherical gas density model consisting of two power laws. The free parameters were the normalization, the inner (α) and outer (β) slopes, the position of the density discontinuity (r_{break}), and the amplitude of the jump (A). The temperature and abundance for each bin were determined from the fits to the projected emission from the coarser bins shown in Figure 9, as there were insufficient counts to perform deprojected spectral fits. The profile from the southwest sector has the typical shape expected for a contact discontinuity. Fitting our model, we find $\alpha = -1.15_{-0.06}^{+0.07}$, $\beta = -0.88_{-0.06}^{+0.06}$, $r_{\text{break}} = 31_{-1}^{+2}$ kpc, and $A = 2.13_{-0.17}^{+0.21}$. In the northeast, the density jump is less pronounced, but still significant within the errors: $\alpha = -0.70_{-0.12}^{+0.11}$, $\beta = -1.47_{-0.15}^{+0.16}$, $r_{\text{break}} = 56_{-5}^{+3}$ kpc, and $A = 1.45_{-0.17}^{+0.22}$. We note that the presence of the long trail of cool gas seen in the northeast in Figure 6 could contaminate the temperature profile shown in Figure 9 (*right*), and therefore affect our fits to the density jump in this region. However, the emissivity is only weakly dependent on the temperature (which does not strongly vary in this region), so the integrated emissivity profile we fit to is dominated by surface brightness variations. Furthermore, if we were able to remove any contribution from the cool arm beyond the surface brightness edge we would raise the overall temperature in this region, which would increase the size of the temperature jump in Figure 9 (*right*) and only strengthen our conclusion that this surface brightness edge corresponds to a cold front. For both the northeastern and southwestern edges, the two power-law model was a much better fit to the data than a single power-law or beta model. The best fit models are plotted in Figure 11.

5.2. *The Dynamical State of NGC 5098*

Based on temperature profiles and fits to the surface brightness profiles (see § 5.1 and § 4.2.2), the edges shown in Figure 1 are identified as cold fronts. Such contact discontinuities are expected to arise during a merger, either at the leading edge of a remnant gas core, or from the sloshing of gas around the potential minimum after it is perturbed by an off-axis encounter with a secondary object (see Markevitch & Vikhlinin 2007 for a review). There are several reasons to identify these features as sloshing fronts. The centers of curvature of the features are roughly centered on the X-ray brightness peak, as expected for sloshing fronts. The density jumps are modest, in the 1.1–2.1 range, in contrast to the larger jumps seen in remnant core cold fronts (e.g., Markevitch et al. 2002; Randall et al. 2009). The spiral structure, seen in both the X-ray surface brightness and temperature maps (Figures 1 & 6), is characteristic of sloshing fronts in existing

observations and simulations (Ascasibar & Markevitch 2006; Dupke et al. 2007; Gastaldello et al. 2009). The apparently nearby galaxy NGC 5098b provides a likely interaction candidate to initiate sloshing in the core of NGC 5098a. Finally, and most compellingly, the temperature map (Figure 7) clearly shows an offset between the cool central gas and the central AGN (and the centroid of the optical emission), which presumably lies at the local minimum of the potential. The structure is very similar to that observed in simulations of gas sloshing (e.g., Figure 7 in Ascasibar & Markevitch 2006).

As noted in § 4.1, one potential problem with this picture is that the cool arm seen in the temperature map (Figure 6) extends well beyond the apparent outer boundary of the surface brightness arm. Detailed spectral fits, described in § 4.2, show that the arm is likely a real feature, and not an artifact of the smoothing inherent in the temperature map. While it is possible that the arm represents sloshed gas from the core of NGC 5098a, the scales involved make this explanation seem unlikely. To explain this feature, we note that NGC 5098b does not show any associated emission in X-rays, implying that this system has been stripped of its gas. The arm seen in the temperature map may be gas stripped from NGC 5098b as it fell into the group from the northeast and interacted with the ambient ICM. The orientation of the arm is consistent with the sloshing interpretation, as the direction of angular momentum implied by the winding direction of the surface brightness spiral arm morphology is consistent with a perturber that has approached from the northeast and passed east of NGC 5098a (in projection). In this scenario, the apparent connection between the outer temperature map arm and the inner surface brightness arm is a projection effect, which may explain the less than perfect correspondence between these features near the tip of the surface brightness arm. Furthermore, it is possible that NGC 5098b, after being ram pressure stripped and passing east of NGC 5098a, circled around NGC 5098a (not necessarily in the plane of the sky) and is now moving roughly to the east, creating a subtle conical wake in the diffuse emission, similar to those seen in the first and last panels of Figure 21 in Ascasibar & Markevitch (2006). The surface brightness arm could be a manifestation of the wake, rather than cool gas sloshed from the core of NGC 5098a, which would explain the lack of correlation with the temperature map. Unfortunately, we do not have enough net counts to test in detail either the interpretation of the extended cool arm in the temperature map as stripped gas from NGC 5098b, or the possibility that the surface brightness arm is a conical wake generated by the return passage of NGC 5098b. We note only that the current data are consistent with either interpretation.

As shown in Figure 4, the central bubbles are swept back to the east of the central AGN in projection. This could be the result of ram pressure due to relative motion between the host galaxy and the ICM either due to the galaxy’s motion within the group or bulk motion of the gas. Alternatively, the jets may have encountered and been deflected by inhomogeneities in the ICM. We note that, in simulations, sloshing fronts are not static features. Rather, gas flows along the spiral arm, from the outer regions into the center (Figure 7 in Ascasibar

& Markevitch 2006). In this system, we therefore expect gas to be flowing inwards from the east, around the the south, and approaching the central AGN from the west. It is therefore possible that the bulk motions in the gas which sweep the central bubbles to the east are due to the velocity field set up in the sloshing front, though we cannot distinguish this possibility from the others previously mentioned.

5.3. The X-ray Cavities

The X-ray surface brightness (Figure 1) and unsharp-masked (Figure 3) images show several statistically significant cavities in the central region of NGC 5098a. In particular, there are two distinct bubbles (seen as X-ray deficits surrounded by rims of bright emission) just north and southeast of the central AGN. The bubbles are the only cavities which correlate with existing radio observations (see § 3.1 and Figure 4), and we focus on these features first.

The bubbles are morphologically similar to features seen in X-ray observations of other galaxies, groups, and clusters. These structures are formed when AGN jets push into the local ICM, evacuating cavities, and often creating bright rims of X-ray emission from the displaced gas. In more evolved remnant cavities the rims tend to be cooler and more dense than the nearby ambient ICM, as in Abell 2052 (Blanton et al. 2003) and Perseus (Fabian et al. 2006), whereas in more recent outbursts they often show higher temperatures associated with shocks, as in NGC 4552 (Machacek et al. 2006), Hercules A (Nulsen et al. 2005), and Centaurus A (Croston et al. 2009). To test for a temperature difference in the rims, we extracted spectra from the northern (brighter) bubble rim and a similar region just outside the rim, subtracted off spectra from local background regions, and fit each with an absorbed APEC model with the abundance fixed at 30% solar. We find best-fitting temperatures of $kT_{\text{rim}} = 0.978^{+0.085}_{-0.096}$ for the rim and $kT_{\text{outside-rim}} = 1.085^{+0.085}_{-0.198}$ just outside the rim. Although the best-fitting temperatures indicate that the rim is somewhat cooler, the difference is not statistically significant.

The proximity of the bubbles to the central AGN, and their relatively small physical size, suggest that they are currently forming as the cavities are inflated by the AGN. If this is the case, one might expect the total pressure in the cavities to be on the order of that in the rims and the surrounding ICM, possibly larger if the cavities are driving shocks. We can estimate the pressure in the X-ray emitting gas in the northern rim using the fit to the spectrum to estimate the temperature and density of the gas. Assuming an edge-on oblate spheroidal geometry for the bubble (with semi-major and minor axes of 3 kpc and 1.6 kpc, respectively), we find an electron density of $n_e \approx 0.03 \text{ cm}^{-3}$ and a pressure of $P_{\text{rim}} \approx 4.5 \times 10^{-11} \text{ dyne cm}^{-2}$. To estimate the pressure inside the bubble, ideally one would like flux measurements from radio observations at multiple frequencies to determine the spectral index of the relativistic particle population. Under the assumption of equipartition, the radio pressure at minimum energy is given by

$$P_{\text{rad}} = \frac{B_{\text{min}}^2}{8\pi} + \frac{4 E_{\text{min}}}{7 \phi V}, \quad (1)$$

where the magnetic field at minimum total energy

$$B_{\text{min}} = [6\pi(1+k)c_{12}(\alpha, \nu_1, \nu_2)L\phi^{-1}V^{-1}]^{2/7}, \quad (2)$$

and the minimum total energy

$$E_{\text{min}} = \frac{7}{4} \left[\frac{1}{6\pi} \phi V (1+k)^{4/3} (c_{12}(\alpha, \nu_1, \nu_2)L)^{4/3} \right]^{3/7}. \quad (3)$$

In these relations, k is the ratio of proton to electron energies, V is the volume of the emitting region, $\phi \approx 1$ is the volume filling factor, L is the radio luminosity at a given frequency, and $c_{12}(\alpha, \nu_1, \nu_2)$ is a parameter (tabulated in Pacholczyk 1970) that depends on the spectral index α and the lower and upper cut-off frequencies, which we take to be $\nu_1 = 10 \text{ MHz}$ and $\nu_2 = 10 \text{ GHz}$. We assume $k \approx 1$, which is expected for a young source since it has not yet had time to entrain material from the ICM. Useful expressions from these relations are given by Govoni & Feretti (2004). Morganti et al. (1997) give 6 cm fluxes of 8.7, 10.3, and 7.1 mJy for the core, the northern lobe, and the southeastern lobe, respectively. Unfortunately, from the literature we were only able to find radio flux measurements for the resolved AGN and lobes at a single frequency, so the value of α inside the lobes is unknown. As a rough estimate, we assume that $\alpha = -1.6$, consistent with results from similar X-ray bubbles in Abell 2052 (Zhao et al. 1993; see Bîrzan et al. 2008 for indices for several sources, though they are given for the total source, not just the lobes, and hence are expected to be steeper). We find an equipartition magnetic field strength of $B_{\text{eq}} \sim 40 \mu\text{G}$ and a minimum radio pressure of $P_{\text{rad}} = 1.5 \times 10^{-10} \text{ dyne cm}^{-2}$, more than three times the X-ray pressure in the rims. However, this result is sensitive to the assumed value of α : if we instead take $\alpha = -1$, which is closer to the value for the bubbles in the Perseus cluster (Pedlar et al. 1990), we find $P_{\text{rad}} = 2.6 \times 10^{-11} \text{ dyne cm}^{-2}$, less than the X-ray pressure in the rims. Morganti et al. (1997) find that the ratio of flux from the northern radio lobe to the total flux from both lobes and the central core is $f \approx 0.43$ at 6 cm (5 GHz). The NRAO/VLA Sky Survey (NVSS, Condon et al. 1998) gives a total flux of 82.9 mJy at 1.4 GHz. Assuming that $f \approx 0.43$ at 1.4 GHz, we find $\alpha \approx -1$. We note that this is an upper limit on α , since the core is expected to be brighter at higher frequencies (e.g., the lobes are not seen in 8.49 GHz X-band images from the VLA archive, whereas the AGN is clearly visible), so that f is a decreasing function of frequency. We therefore conclude that $P_{\text{rad}} > 2.6 \times 10^{-11} \text{ dyne cm}^{-2}$ is a hard lower limit, and the radio pressure in the northern bubble is on the order of the pressure in the surrounding X-ray emitting rims. The fact that pressures are roughly equal under the assumption that $k = 1$, and that the bubbles are physically close to the AGN, suggest that the bubbles are young features, possibly currently being inflated by the central AGN. Follow-up high-resolution radio observations, along with deep X-ray observations, would be of interest for a better comparison of the relative pressures in the rims and bubbles, and of the X-ray temperature in the rims and the ambient ICM.

The unsharp-masked image (Figure 3) shows several surface brightness depressions beyond the inner bubbles. All are within the surface brightness edge shown in Fig-

ure 1. Although these depressions show no correlation with the existing radio data, some of them are more statistically significant than the depressions associated with the bubbles, which are clearly real and seen in radio observations. We therefore make the assumption that these features are “ghost cavities”, leftover from previous AGN outbursts, devoid of X-ray emitting gas but no longer strongly emitting in the radio, as seen in other systems (e.g., Jetha et al. 2008). We estimate the total volume occupied by the cavities by extracting spectra from the central $30''$ (22 kpc), with and without including the regions of the cavities, and fitting with an absorbed APEC model. Comparing the volume emissivities (calculated from the area-normalized normalizations of the fits) directly gives an estimate for the fraction of the total volume occupied by the cavities. We find a total cavity volume of 1240 kpc^3 for 14 cavities within the central 22 kpc (i.e., a filling-factor of about 3%), giving an average cavity volume of 31 kpc^3 (note that not all of these cavities are visible in Figure 3, as some are within the large dark feature to the east that corresponds to an edge in the central surface brightness, and are not visible at this scaling and contrast). For spherical cavities, this gives an average radius of $\sim 2 \text{ kpc}$, fully consistent with the average projected cavity radius (even though several cavities are clearly non-spherical) and with our assumption that the cavities contain no X-ray emitting gas. Assuming that the bubbles rise buoyantly at the sound speed in the gas, $c_s \approx 460 \text{ km s}^{-1}$ for $kT = 0.8 \text{ keV}$, the average distance of the bubbles from the AGN $d_{\text{avg}} = 9 \text{ kpc}$ gives an average cavity age of $t_{\text{age}} \approx 18 \text{ Myr}$.

The mechanical energy input required to inflate the cavities, E_{mech} , can be estimated from the X-ray gas pressure and the total volume occupied by the cavities. Using the density and temperature from the spectral fit to the central 22 kpc, we find an average pressure of $\sim 1.8 \times 10^{-11} \text{ dyne cm}^{-2}$, which gives a total mechanical energy input of $E_{\text{mech}} \approx 7 \times 10^{56} \text{ ergs}$, consistent with what is found in other galaxy groups (McNamara 2004). We obtain an estimate for the cooling rate of the central gas from the 0.3–12 keV X-ray luminosity in the same region, which we find from our fitted spectral model to be $L_X = 1.5 \times 10^{42} \text{ ergs s}^{-1}$. The mechanical energy in the cavities is therefore sufficient to offset cooling in the diffuse gas for 15 Myr, very similar to what was found for the Virgo galaxy NGC 4552 (Machacek et al. 2006), and similar to the average cavity age calculated from the rise time above. This is on the order of central AGN cycle times inferred for other galaxy clusters (e.g., Blanton et al. 2009; Clarke et al. 2009) of a few tens of Myrs. We therefore conclude that the current average mechanical luminosity of the AGN is nearly if not completely

sufficient to balance radiative cooling of the gas in the central region (we also note that the total energy in the bubbles may be up to a factor of 2–4 times more than the mechanical energy alone, see McNamara 2004).

6. SUMMARY

We have analyzed *Chandra* ACIS-S3 observations of the NGC 5098 galaxy group. X-ray images reveal a spiral arm morphology extending to the northeast, a sharp edge in the diffuse emission surrounding much of NGC 5098a and connecting to the outer boundary of the arm, as well as bubbles and other X-ray surface brightness depressions in the core. Temperature and density profiles across the edges indicate that they are cold fronts. The structure of the cold fronts (which have relatively modest density jumps, and radii of curvature centered on the peak of the diffuse emission), the spiral structure seen in the X-ray surface brightness and temperature maps, and the offset between the central clump of cool gas seen in the temperature map from the central AGN and optical center of the galaxy all point to gas sloshing in the core, as seen in simulations and other observations. The obvious candidate perturber is the nearby galaxy NGC 5098b, which has apparently been stripped of its X-ray emitting gas. We have suggested that the long outer arm of cool gas seen in the temperature map may in part be the stripped tail of NGC 5098b, formed as it passed through the group ICM and initiated sloshing in NGC 5098a. The winding direction of the inner spiral arm is consistent with the perturber approaching from the northeast to the southeast, which matches the trajectory implied for NGC 5098b if we interpret the extended temperature map arm as its stripped tail. The two bubbles in the core of NGC 5098a, which are seen as X-ray cavities surrounded by bright rims of emission, correlate with radio observations. A comparison of the radio pressure in the bubbles to the X-ray pressure in the rims shows that they are about equal, consistent with these being young features that are currently being inflated by jets from the central AGN. We make the assumption that the other X-ray cavities seen in the core are ghost cavities, left over from previous AGN outbursts. An estimate of the mechanical energy required to inflate these cavities shows that the energy output of the central AGN is sufficient to balance radiative cooling of the gas in this region.

The financial support for this work was partially provided for by the Chandra X-ray Center through NASA contract NAS8-03060, and the Smithsonian Institution. We thank the anonymous referee for useful comments.

REFERENCES

- Adelman-McCarthy, J., et al. 2008, *ApJS*, 175, 297
 Ascasibar, Y., & Markevitch, M. 2006, *ApJ*, 650, 102
 Birzan, L., McNamara, B. R., Nulsen, P. E. J., Carilli, C. L., & Wise, M. W. 2008, *ApJ*, 686, 859
 Blanton, E. L., Randall, S. W., Douglass, E. M., Sarazin, C. L., Clarke, T. E. & McNamara, B. R. 2009, *ApJL*, submitted
 Blanton, E. L., Sarazin, C. L., & McNamara, B. 2003, *ApJ*, 585, 227
 Buote, D. A. 2000, *MNRAS*, 311, 176
 Clarke, T. E., Blanton, E. L., Sarazin, C. L., Anderson, L. D., Gopal-Krishna, Douglass, E. M., Kassim, N. E. 2009, *arXiv:0904.1610*
 Colla, G., et al. 1970, *A&AS*, 1, 281
 Condon, J. J., Cotton, W. D., Greisen, E. W., Yin, Q. F., Perley, R. A., Taylor, G. B., & Broderick, J. J. 1998, *AJ*, 115, 1693
 Croston, J. H. et al. 2009, *arXiv:0901.1346*
 Davis, D. S., Mulchaey, J. S., & Mushotsky, R. F. 1999, *ApJ*, 511, 34
 Dupke, R., White, R. E., & Bregman, J. N. 2007, *ApJ*, 671, 181
 Fabian, A. C., Sanders, J. S., Taylor, G. B., Allen, S. W., Crawford, C. S., Johnstone, R. M., Iwasawa, K. 2006, *MNRAS*, 366, 417
 Gastaldello, F., Buote, D. A., Humphrey, P. J., Zappacosta, L., Bullock, J. S., Brighenti, F., & Mathews, W. G. 2007, *ApJ*, 669, 158

- Gastaldello, F., Buote, D. A., Temi, P., Brighenti, F., Mathews, W. G., & Ettori, S. 2009, *ApJ*, 693, 43
- Gitti, M., McNamara, B. R., Nulsen, P. E. J., Wise, M. W. 2007, *ApJ*, 660, 1118
- Govoni, F. & Feretti, L. 2004, *IJMPD*, 13, 1549
- Hwang, U., Mushotzky, R. F., Burns, J. O., Fukazawa, Y., & White, R. A. 1999, *ApJ*, 516, 604
- Jethava, N. N., Hardcastle, M. J., Babul, A., O'Sullivan, E., Ponman, T. J., Raychaudhury, S., Vrtilak, J. 2008, *MNRAS*, 384, 1344
- Machacek, M., Nulsen, P. J. E., Jones, C., & Forman, W. R. 2006, *ApJ*, 648, 947
- Mahdavi, A., Böhringer, H., Geller, M. J., & Ramella, M. 2000, *ApJ*, 534, 114
- Mahdavi, A., Finoguenov, A., Böhringer, H., Geller, M. J., & Henry, J. P. 2005, *ApJ*, 622, 187
- Markevitch, M., Gonzalez, A., David, L., Vikhlinin, A., Murray, S., Forman, W., Jones, C., & Tucker, W. 2002, *ApJL*, 567, 27
- Markevitch, M., & Vikhlinin, A. 2007, *PhR*, 443, 1
- Mazzotta, P., Markevitch, M., Vikhlinin, A., Forman, W. R., David, L. P., & VanSpeybroeck, L. 2001, *ApJ*, 555, 205
- McNamara, B. R. 2004, *Clusters of Galaxies: Probes of Cosmological Structure and Galaxy Evolution* (Carnegie Observatories, Pasadena)
- McNamara & Nulsen, 2007, *ARA&A*, 45, 117
- Morganti, R., Parma, P., Capetti, A., Fanti, R., de Ruiter, H. R., & Prandoni, I. 1997, *A&A*, 126, 335
- Nulsen, P. J. E., Hambrick, D. C., McNamara, B. R., Rafferty, D., Birzan, L., Wise, M. W., & David, L. P. 2005, *ApJ*, 625, L9
- Pacholczyk, A. G. 1970, *Radio Astrophysics* (W. H. Freeman & Co., San Francisco)
- Parma, P., de Ruiter, H. R., Fanti, C., Fanti, R. 1986, *A&AS*, 64, 135
- Pedlar, A., Ghataure, H. S., Davies, R. D., Harrison, B. A., Perley, R., Crane, P. C., & Unger, S. W. 1990, *MNRAS*, 246, 477
- Peterson, J. R., & Fabian, A.C. 2006, *Physics Reports*, 427, 1
- Ramella, M., Geller, M. J., & Huchra, J. P. 1989, *ApJ*, 344, 57
- Ramella, M., Geller, M. J., Huchra, J. P., & Thorstensen, J. R. 1995, *AJ* 109, 1458
- Randall, S., Jones, C., Kraft, R., Forman, W. R., & O'Sullivan, E. 2009, *ApJ*, 696, 1431
- Randall, S., Nulsen, P., Forman, W., Jones, C., Machacek, M., Murray, S., & Maughan, B. 2008, *ApJ*, 688, 208
- Sambruna, R. M., Eracleous, M., & Mushotzky, R. F. 1999, *ApJ*, 526, 60
- Smith, J., et al. 2002, *AJ*, 123, 2121
- Sun, M., Voit, G. M., Donahue, M., Jones, C., Forman, W., & Vikhlinin, A. 2009, *ApJ*, 693, 1142
- Xue, Y.-J., Böhringer, H., & Matsushita, K. 2004, *A&A*, 420, 833
- Zhao, J.-H., Sumi, D. M., Burns, J. O., & Duric, N. 1993, *ApJ*, 416, 51

TABLE 1
SPECTRAL FITS

Region #	kT (keV)	Abund. (solar)	χ^2/dof	Net Cnts.
R1	$0.934^{+0.014}_{-0.014}$	$0.30^{+0.04}_{-0.03}$	50.2/50=1.00	3743
R2	$0.768^{+0.045}_{-0.058}$	$0.17^{+0.11}_{-0.07}$	3.6/7=0.82	554
R3	$0.813^{+0.043}_{-0.051}$	$0.20^{+0.13}_{-0.08}$	2.8/7=0.90	484
R4	$0.993^{+0.030}_{-0.033}$	$0.26^{+0.11}_{-0.08}$	4.7/7=0.69	793
R5	$1.223^{+0.046}_{-0.054}$	$0.58^{+0.28}_{-0.18}$	6.55/7=0.48	687
R5	$1.147^{+0.056}_{-0.060}$	(0.26)	11.1/8=1.38	687
R6	$1.056^{+0.066}_{-0.042}$	$0.13^{+0.04}_{-0.03}$	27.8/32=0.68	791
R7	$1.298^{+0.062}_{-0.076}$	$0.20^{+0.06}_{-0.08}$	25.5/18=1.42	546

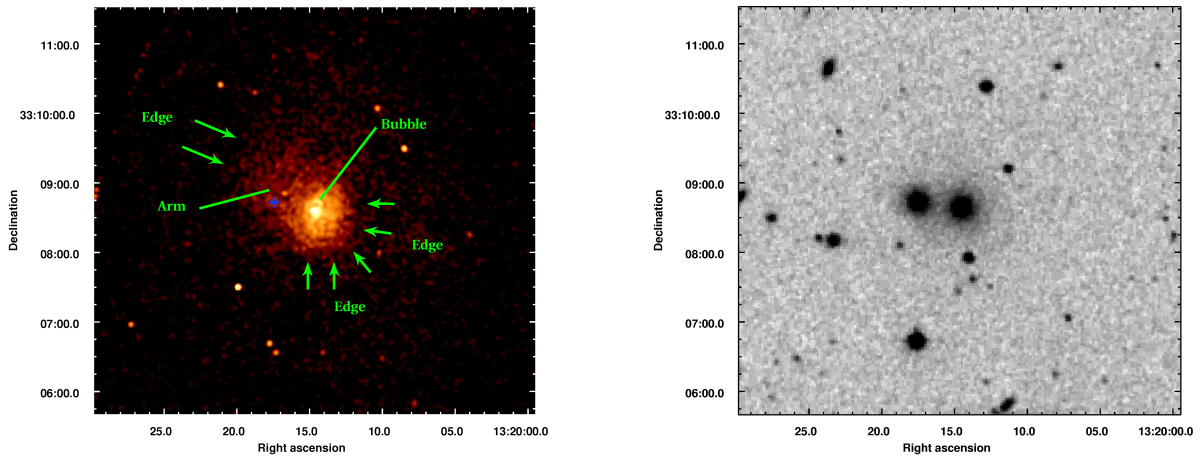


FIG. 1.— *Left Panel:* Exposure corrected, background subtracted 0.6–5 keV *Chandra* ACIS-S3 observation of NGC 5098. The image has been smoothed with an $3''$ radius gaussian. Regions with less than 10% of the total exposure were omitted. The image shows a spiral arm structure to the northeast, a sharp surface brightness edge beginning in the west and connecting around the south to the outer boundary of the arm, and central bubbles surrounded by bright rims of emission. The blue cross marks the optical position of NGC 5098b. *Right Panel:* DSS image of the same field. NGC 5098a is the western galaxy of the central bright galaxy pair while NGC 5098b is to the east.

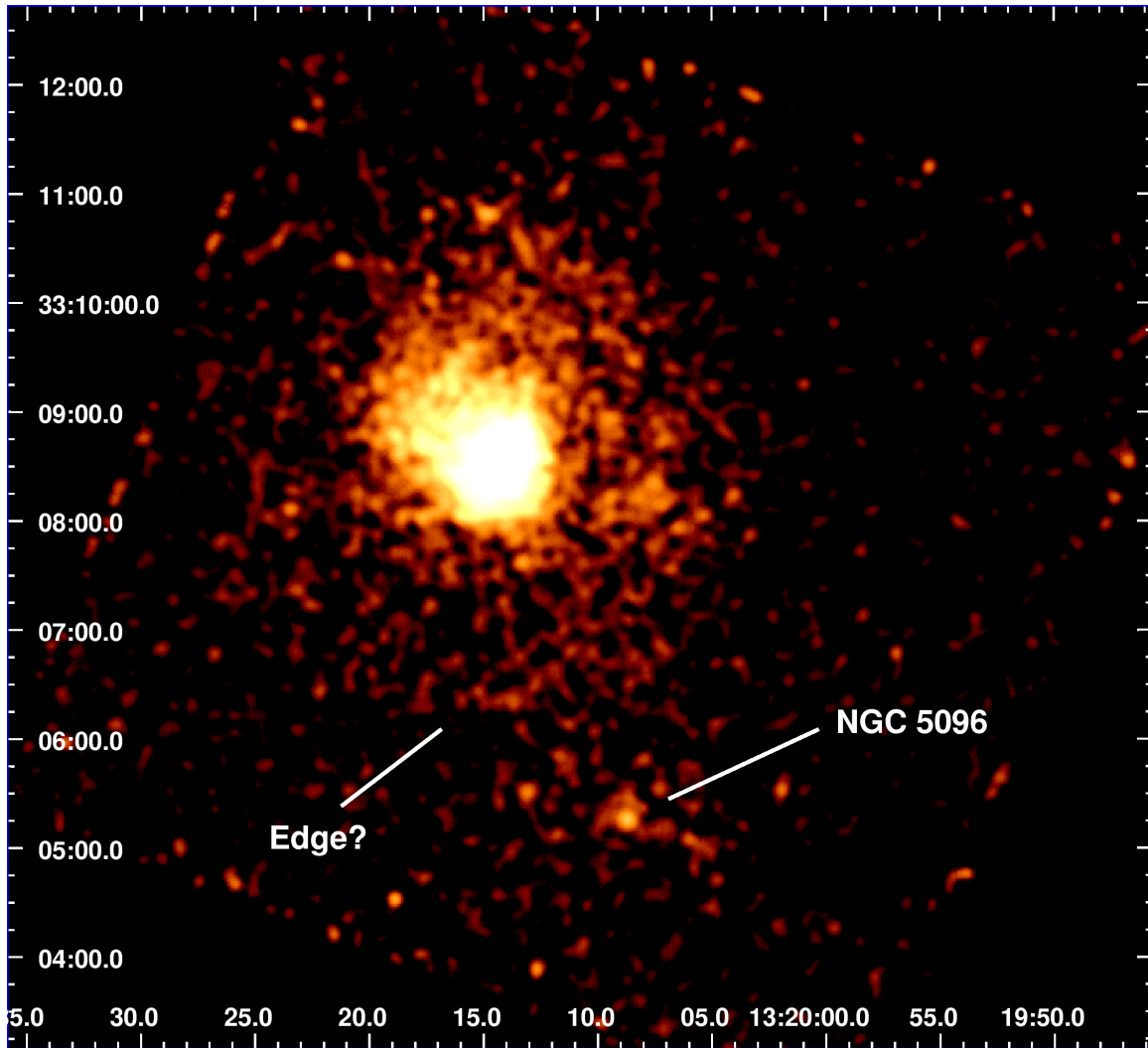


FIG. 2.— The 0.6–5.0 keV *Chandra* image, smoothed with a 12'' radius gaussian to better show faint, diffuse emission at large radii. Point sources have been removed, as described in the text (see § 3). There is a sharp, linear edge in the emission to the south. Diffuse emission from the group member NGC 5096 is seen to the southwest.

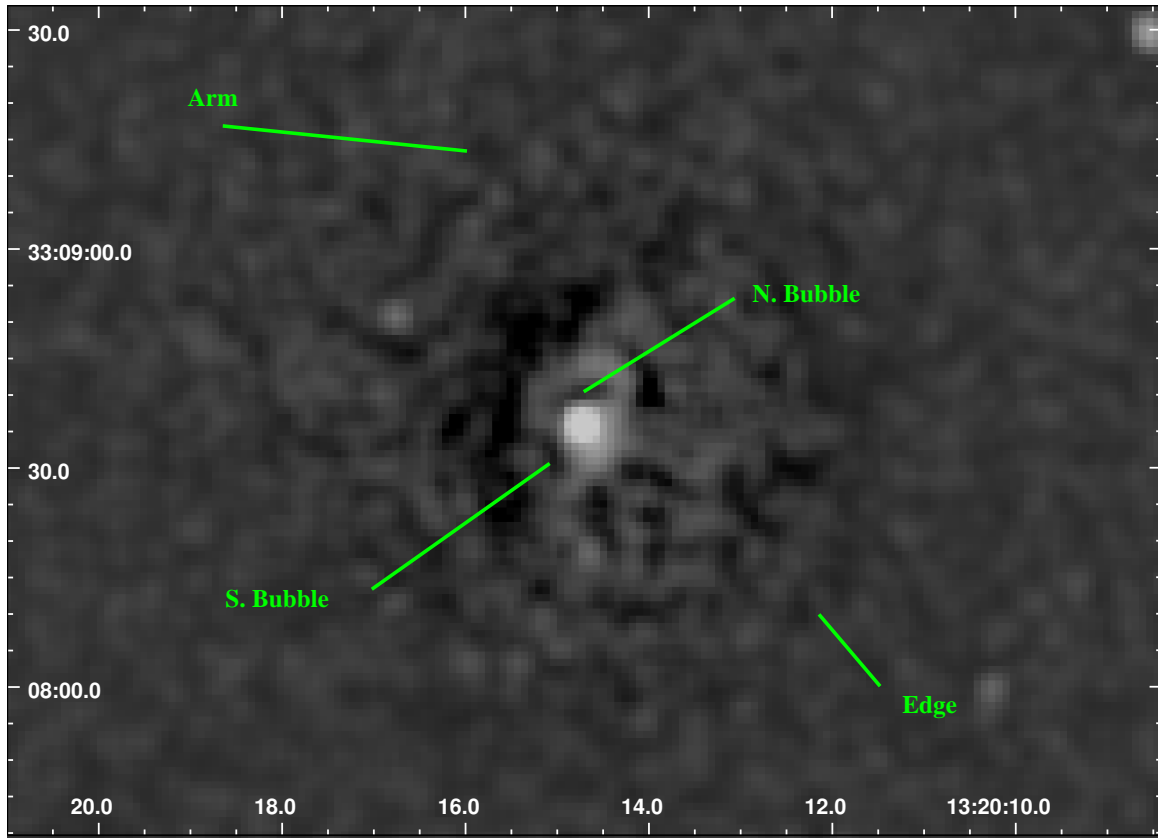


FIG. 3.— An unsharp-masked 0.3–5 keV image of the central region of NGC 5098a. X-ray cavities, or bubbles, encompassed by bright rings of emission are clearly seen to the north and southwest of the AGN. The bubbles are filled with radio-emitting plasma (see Figure 4). The unsharp-masking reveals other fine structure and surface brightness depressions, particularly in the southwest (all within the surface brightness edge shown in Figure 1).

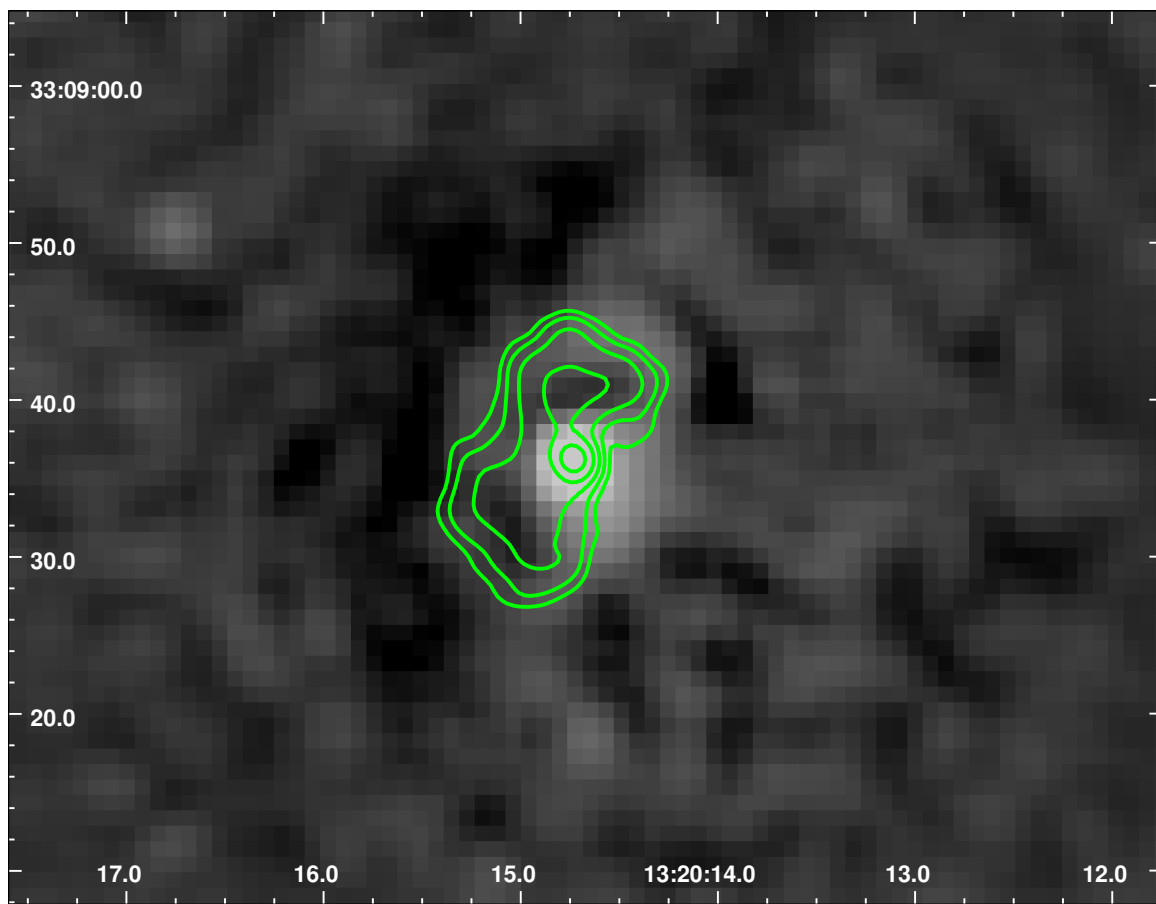


FIG. 4.— A close-up of the bubbles shown in Figure 3. The logarithmically-spaced contours were generated from 1.45 GHz VLA L-band images taken from the VLA data archive. Radio emission fills the X-ray bubbles.

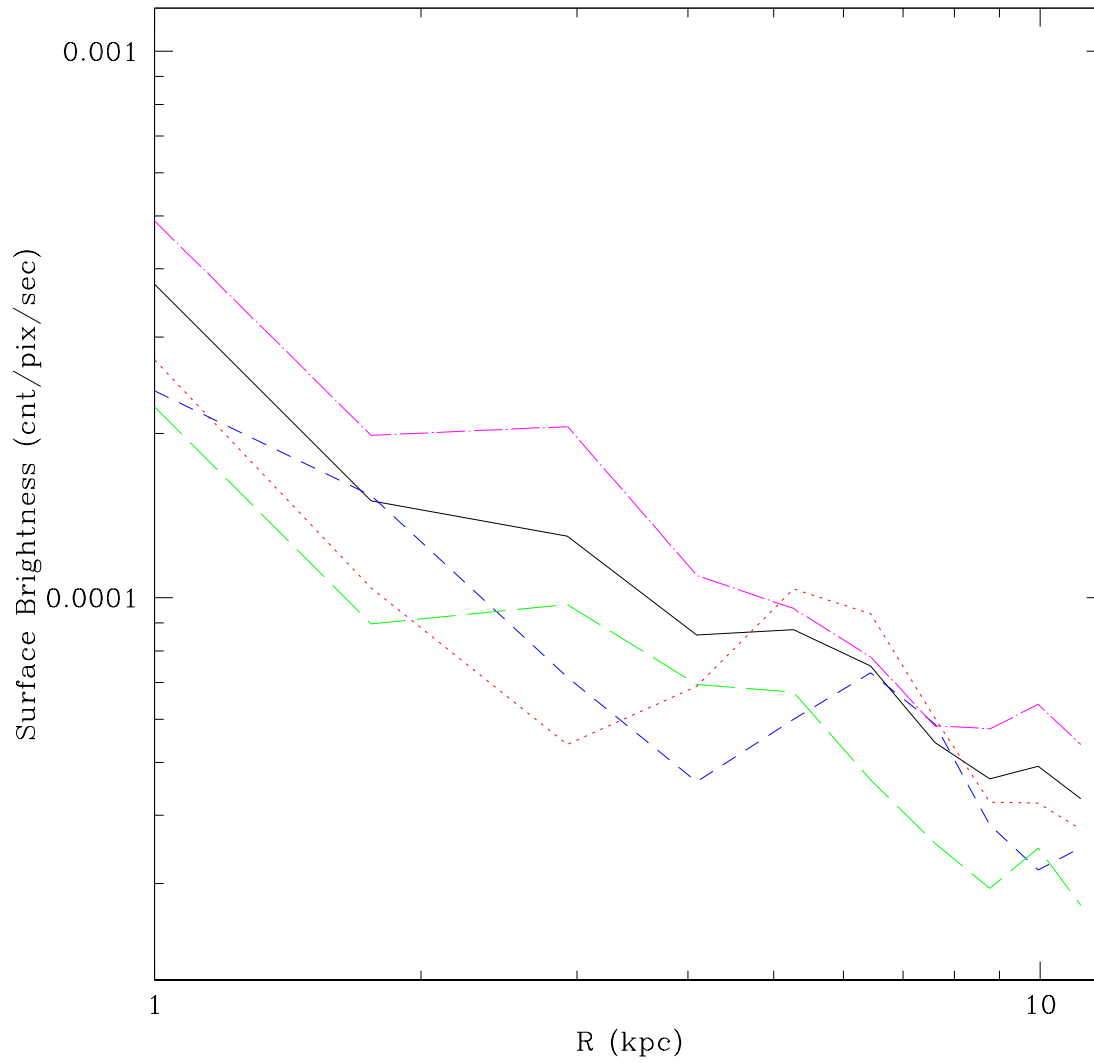


FIG. 5.— The 0.6-5.0 keV surface brightness profile in four sectors containing the northern bubble (red dotted), the southern bubble (blue short-dashed), the region to the east (green long-dashed), and the region to the west (magenta dot-dashed) as compared to the azimuthal average (black solid). Error bars have been omitted for clarity. The peaks at ~ 6 kpc correspond to the bright bubble rims, and the deficits at 3-4 kpc to the bubbles themselves. The overall east-west asymmetry is also evident. Pixels are $0.98'' \times 0.98''$.

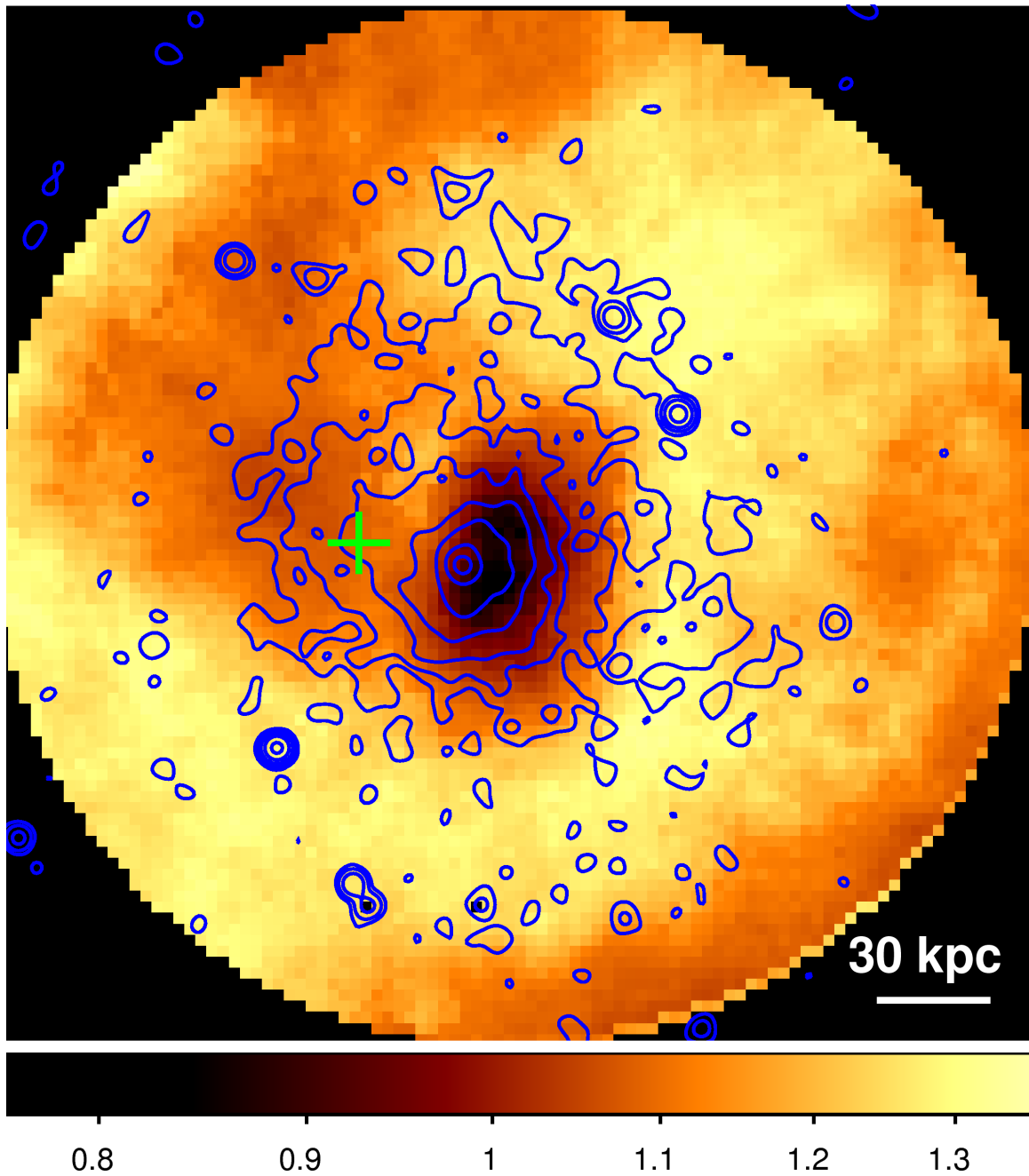


FIG. 6.— Temperature map derived from the ACIS-S3 data, with *Chandra* X-ray logarithmic surface brightness contours overlaid. The green cross indicates the optical position of NGC 5098b. The color-bar gives the temperature in keV.

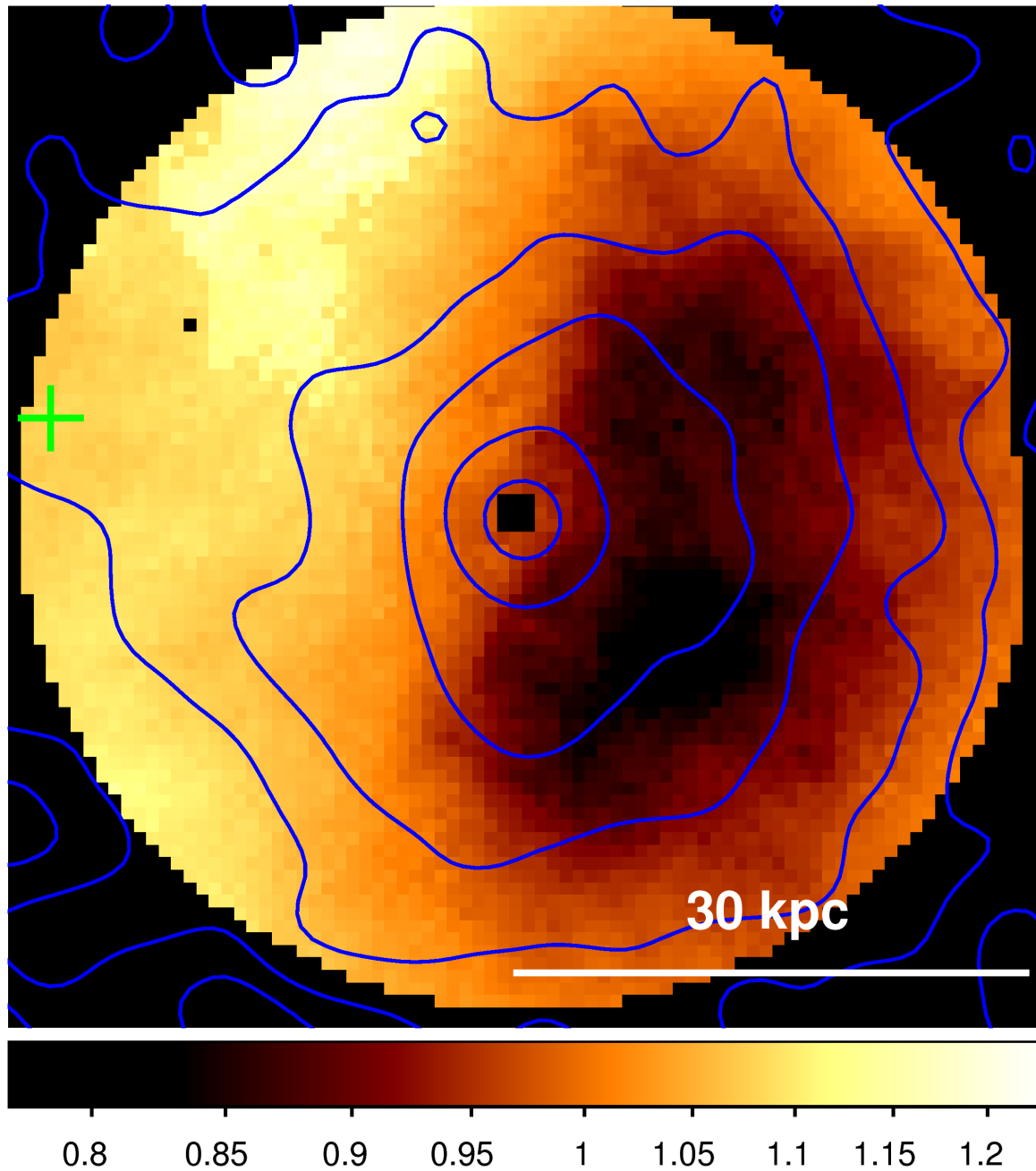


FIG. 7.— A higher resolution temperature map of the central region of NGC 5098a, with the same X-ray surface brightness contours overlaid as in Figure 6. The green cross indicates the optical position of NGC 5098b. The elliptical cool region to the west is split into two cool spots, one to the north and one to the south. The holes in the temperature map indicate pixels that were completely contained within an excluded source region (e.g., at the central AGN).

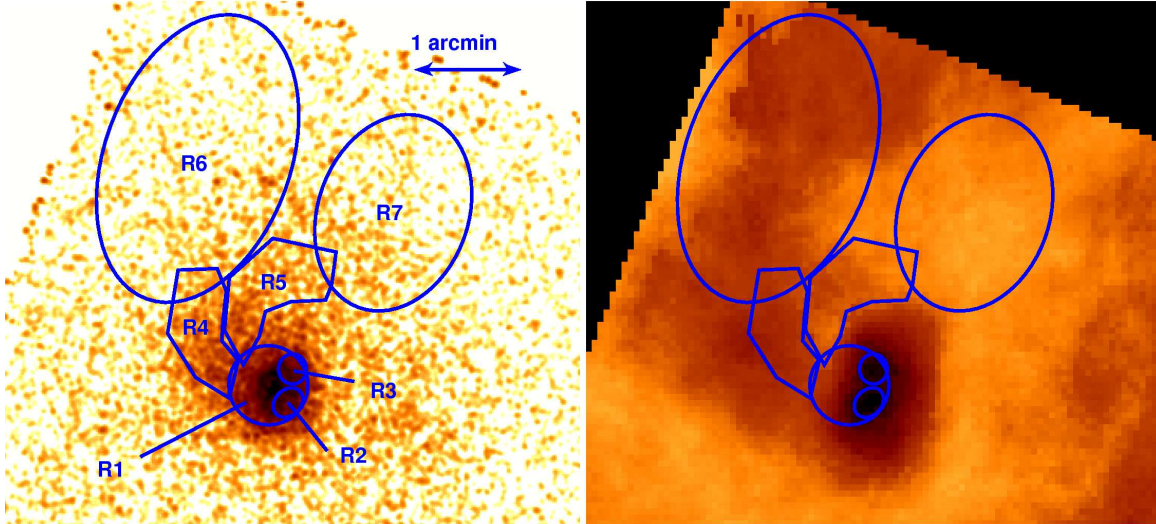


FIG. 8.— The regions fitted in Table 1 overlaid on the 0.6 – 5.0 keV *Chandra* image (*left*) and temperature map (*right*). The image has been smoothed with a $6''$ radius gaussian, and the point sources have been removed by filling in source regions as described in the text (§ 4.2).

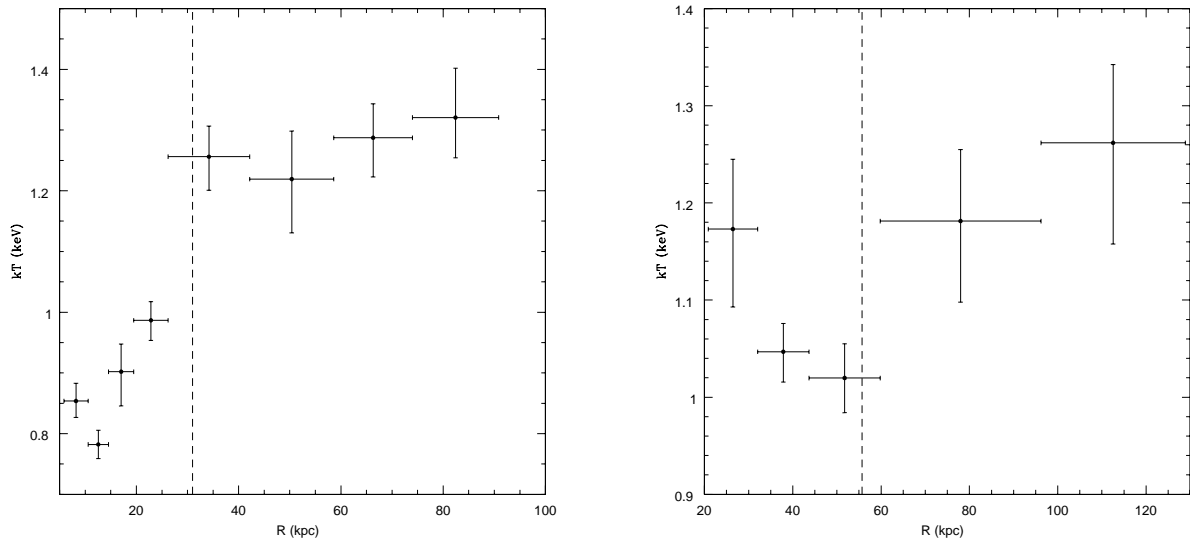


FIG. 9.— Temperature profiles to the southwest (*left*) and northeast (*right*) for the semi-annular areas shown in Figure 10 (but with fewer, larger bins). The dashed lines mark the positions of the density jumps calculated in § 5.1.

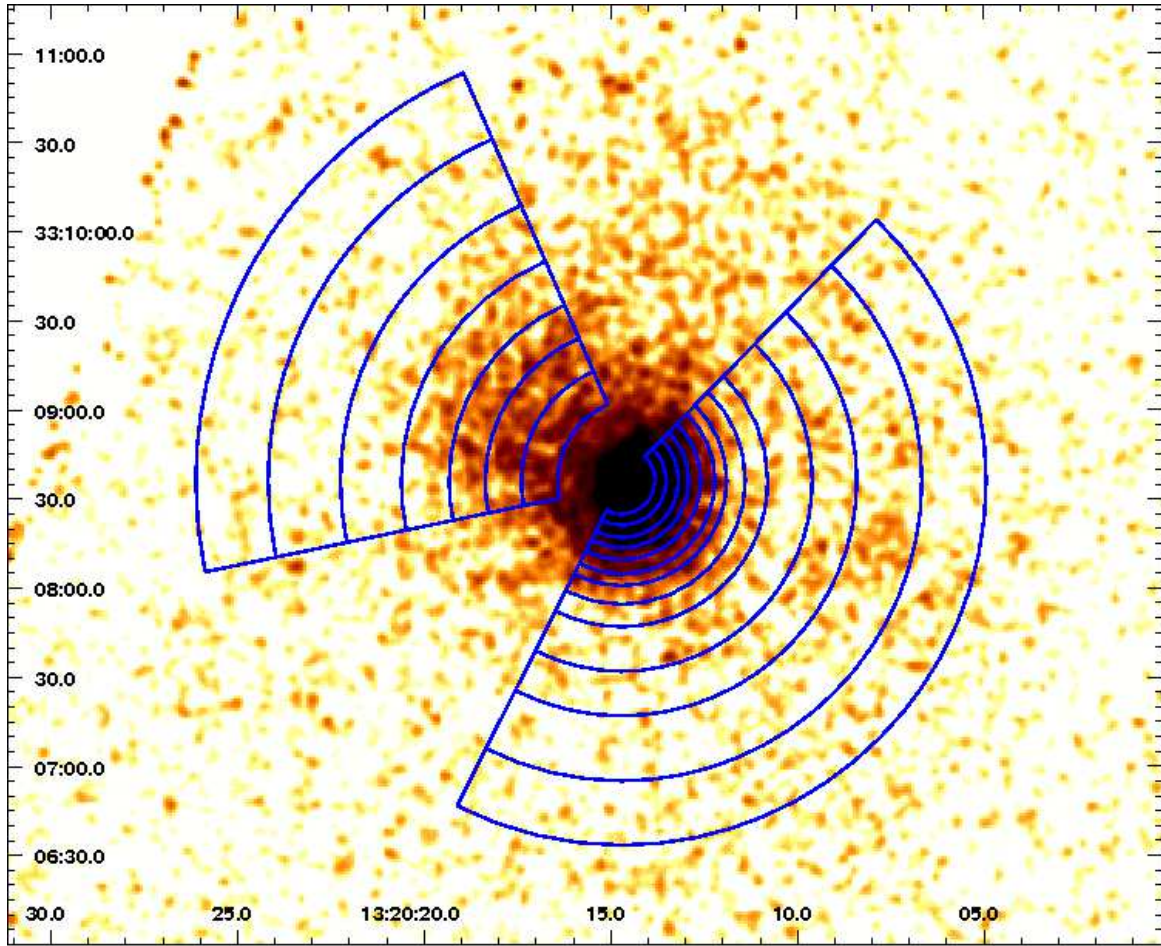


FIG. 10.— Regions used to generate the projected emission measure profiles shown in Figure 11 overlaid on the background subtracted, exposure corrected, smoothed, 0.6 – 5.0 keV *Chandra* image (with point sources removed).

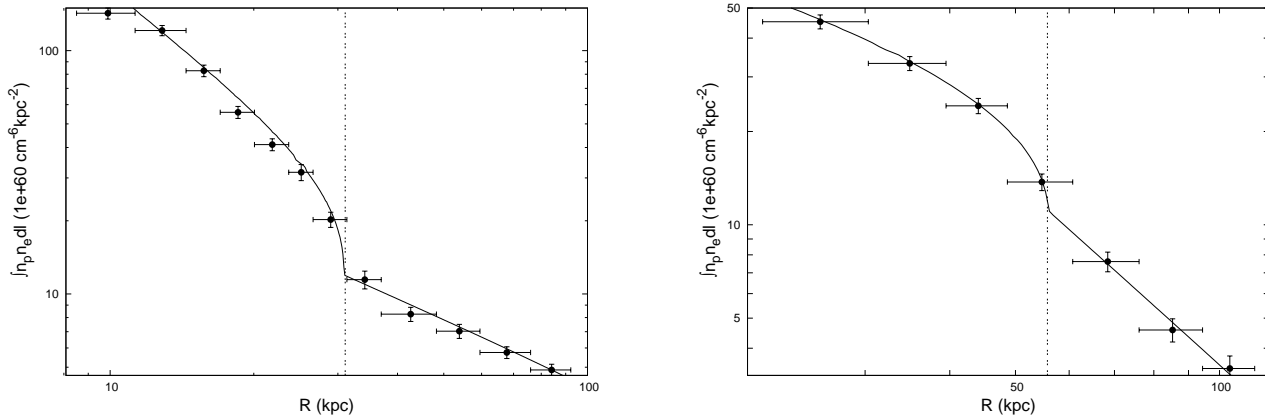


FIG. 11.— *Left Panel*: Integrated emission measure profile extracted from the southwestern region shown in Figure 10. The x-axis gives the radius from the apparent center of curvature defined by the feature. The best fit two power law density jump model is given by the solid line. The vertical dashed line shows the best fit location of the density discontinuity. *Right Panel*: Same for northeastern region in Figure 10.